Applied Acoustics 218 (2024) 109862

Contents lists available at ScienceDirect

Applied Acoustics

journal homepage: www.elsevier.com/locate/apacoust

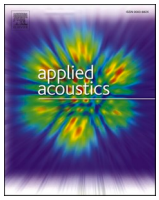

Curve squeal in sharp curves: effect of multiple wheel/rail contact points

Federico Castellini [a,*], Leonardo Faccini [a], Egidio Di Gialleonardo [a], Stefano Alfi [a], Roberto Corradi [a], Giacomo Squicciarini [b], David Thompson [b]

[a] Politecnico di Milano, Department of Mechanical Engineering, Via Giuseppe La Masa 1, 20156, Milano, Italy
[b] ISVR, University of Southampton, Southampton SO17 1BJ, United Kingdom

ARTICLE INFO

Keywords:
Curve squeal
Frequency-domain model
Multiple contact points
Tramways

ABSTRACT

Curve squeal is one of the most annoying noise problems related to the operation of trains, trams, and metros in urban environments. It typically occurs in sharp curves, which are very common in urban areas, and is disturbing for both passengers and people in proximity to the line. Curve squeal is characterized by a loud tonal noise that usually occurs close to the natural frequencies of the wheel. It is generally attributed to the self-excited vibration of the wheel, as a result of the contact phenomena taking place at the wheel/rail interface during curve negotiation. An experimental campaign has been carried out on a sharp tramway curve to measure noise emission due to curve squeal. This revealed that different squealing frequencies and noise levels were generated by two different tramcars of the same type. The presence of a second contact point between the flange back of the leading inner wheel of one of the tramcars and the groove rail was found to be the reason behind these dissimilar experimental results. Thus, the aim of this work is to assess the role of the flange back contact condition on the excitation of squeal noise. A curve squeal prediction model is formulated in the frequency domain to include the presence of multiple wheel/rail contact patches. Numerical simulations reveal that this contact condition can significantly alter the squealing frequencies involved, similarly to what is observed in the pass by sound pressure measurements. The contact on the flange back is found to promote mode-coupling mechanisms in the proximity of close pairs of wheel vibration modes. These results suggest that the potential presence of multiple contacts between wheel and rail should be considered to obtain reliable curve squeal predictions.

1. Introduction

Curve squeal noise is a loud and very annoying tonal noise, which often occurs when a rail vehicle negotiates a tight curve. Different mechanisms have been proposed in past research to describe the root causes of the physical phenomenon. The most common is the wheel/rail self-excitation caused by the falling behaviour of the friction curve in fully sliding conditions. A negative slope of the friction curve provides a negative equivalent damping to the wheel/rail system, which may result in the so called “wheel self-excited vibration” [1,2]. Other mechanisms such as mode coupling and flange contact have also been evaluated as possible sources of curve squeal.

As far as mode coupling is concerned, the friction force acts as a coupling force between the motions in the directions normal and tangential to the contact surface. In other words, velocity dependent forces (the friction forces in this specific case) modify the characteristics of the system, coupling the natural frequencies of two close structural modes, resulting in an unstable behaviour of the system [3,4].

As observed experimentally in [5,6], the mode coupling type of instability usually results in a phase difference between the vertical and the lateral fluctuations. This type of instability can also be identified experimentally by looking at the shift in the frequencies involved in the squeal phenomena with respect to the wheel natural frequencies [5].

A thorough literature review of the several experimental and numerical investigations concerning curve squeal is provided by Thompson et al. in [7]. The review presents the possible techniques that can be adopted to predict the curve squeal occurrence and summarises the experimental evidence obtained in the last few decades. Curve squeal predictions can be carried out using either frequency- or time-domain formulations. In the former, the system is linearised for small fluctuations in friction force about the steady-state curving condition and the stability of the linearised system is studied to determine potential unstable frequencies. In the latter, the nonlinear equations are solved directly in the time domain. A model in the frequency-domain that

* Corresponding author.
E-mail address: federico.castellini@polimi.it (F. Castellini).

https://doi.org/10.1016/j.apacoust.2024.109862
Received 11 September 2023; Received in revised form 12 December 2023; Accepted 5 January 2024
Available online 30 January 2024

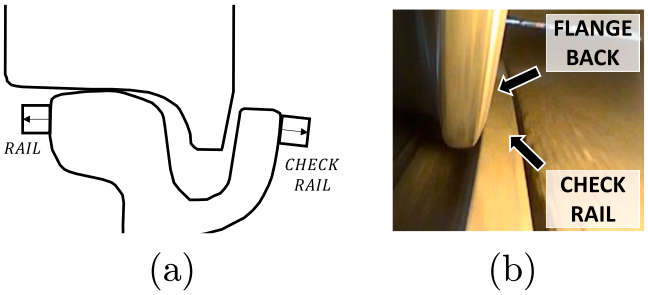

Fig. 1. (a) Placement of sensors on the rail and (b) an example of flange back contact condition recorded by the on-board camera.

includes vibration in the lateral and vertical directions was proposed by De Beer et al. [8] and extended by Huang [9] to consider also longitudinal and spin dynamics. The model was further extended by Squicciarini et al. [10] to include the simultaneous presence of multiple contact points between the wheel and rail. The role of the track dynamics and its conditions has been investigated theoretically in [11,12] and experimentally in [13,14]. A twin-disc rolling contact test rig was adopted by Meehan and Liu to characterize the slope of the friction-creep curve in different contact conditions and to assess the effectiveness of friction modifiers on curve squeal noise mitigation [15].

Concerning the time-domain analysis, different modelling approaches have been adopted. These can firstly be based on the integration of the equations of motion describing the wheel/rail dynamics, as done in [9,16,17]. Formulations, which include the wheel and rail dynamics using Green's functions, were developed in [18,19] for single and multiple contact points. A comprehensive model of the railway wheelset-track interaction in curves was developed by Martinez-Casas et al. [20], in which the equation of motion of the entire wheelset Finite Element Model (FEM) is coupled with the track by means of a pre-tabulated multi-Hertzian contact model. The results reported in [21] suggest the possible occurrence of curve squeal also in the presence of constant friction conditions, as obtained also in [22]. A time-domain formulation, including acoustic predictions, was presented by Lai et al. adopting a FE model and modal reduction techniques [23].

The research described in this work has been motivated by measurements undertaken on a modern low-floor tramcar traversing a tight curve. These revealed that an additional contact point existed between the flange back of the leading inner wheels of the bogie and the check rail part of the groove rail. This may have a strong influence on the curve squeal noise levels and frequencies. The aim of the present work is to assess the role of this contact condition on the excitation of squeal noise. A wheel/rail coupled model in the frequency domain is adopted, including the possible presence of multiple wheel/rail contact points. The system is linearized about the steady-state curving condition, which is identified by multibody simulations of the tramcar vehicle dynamics during the negotiation of the reference curve. Experimental Modal Analysis (EMA) and impact tests were adopted to introduce in the model the actual high-frequency wheel and rail dynamics, including cross contributions between different contact points. Due to uncertainty in the environmental and wheel/rail contact conditions, that are the main factors behind curve squeal, the frequency-domain formulation adopted includes statistical variability at the wheel/rail interface. The model is used to identify the frequencies at which the vehicle is most prone to squeal. Numerical simulations under single and multiple wheel/rail contact conditions are qualitatively compared with the squeal noise measurements. This shows that the curve squeal predictions obtained using this computationally efficient methodology give good agreement with the measurements, highlighting the difference between single and multiple contact points.

The paper is organized as follows: the experimental evidence that motivated this work is summarised in Section 2. In Section 3, experimental evidence is compared with the results obtained through multibody simulations of the reference tramcar. The modelling approach adopted to carried out curve squeal prediction is formulated in Section 4, while the methodology adopted to introduce wheel and rail mobilities is described in Section 5. The curve squeal noise measurements of Section 2 are compared with the predictions in Section 6. Finally, concluding remarks are given in Section 7.

2. Curve squeal noise measurements

An experimental campaign was carried out to measure the noise emission and rail vibration due to curve squeal. Pass-by noise measurements were performed on a reference curve (radius 24 m), negotiated by tramcars travelling at a constant speed of 10 km/h. The curve had been recently renovated and fitted with a new embedded track with groove rails. A cross-section of the curve was monitored with two accelerometers mounted on the side of the rail head and on the check rail part of the groove rail (see Fig. 1a). Rail vibration on the check rail was analysed to detect flange-back contacts during curve negotiation. An example of flange-back contact condition filmed by an on-board camera mounted during one of the tests is shown in Fig. 1b. A microphone placed on the inner side of the curve, at a lateral distance of 2.5 m from the centre of the track, was used to measure the sound pressure generated by the tramcar during curve negotiation.

The noise emission of three different tramcars of the same types was recorded during the experimental campaigns. All these trams are modern low-floor articulated units, with seven car bodies: four are each mounted on a single bogie, while the other three are suspended between the four bogied ones. The trams are equipped with independently rotating resilient wheels. Three passages of vehicle (a) and single passages of vehicle (b) and vehicle (c) were recorded. All tramcars were found to generate strong and persistent curve squeal noise emission while negotiating the same curve a short time apart. Despite similar squealing characteristics were expected by tramcars of the same type negotiating the same curve in almost identical environmental conditions, measured noise levels highlighted that the three passages of vehicle (a) always result into squeal close to 550 Hz and 2500 Hz while vehicle (b) and vehicle (c) result into dominant noise emission mainly close to 1500 Hz and 2500 Hz.

Noise signals are further analysed by separating noise contribution in different frequency intervals. Measured squealing frequencies are found to be close to one-third octave bands lower/upper limits. Thus, data are collected into pairs of adjacent one-third octave bands that include the most important frequencies associated to a squealing event. For example, to capture the squeal noise events in the range 1200–1500 Hz the measured signals are filtered between 1130 and 1760 Hz.

For all the vehicle passages available (five in total), the noise signals have been filtered in four frequency bands, corresponding to the most important squealing frequencies measured, and the L_{eq} over a 5 s moving window is evaluated in each of these bands. For every 0.5 s time windows the four bands are ranked in order of importance by comparing

their level with the overall noise. This provides a straightforward hierarchy, on a ranking scale from 1 to 4, that quantifies the extent of the band's influence on the overall noise. In addition, the relative amount of time each band is found to be in a certain rank has been calculated. For example, if a frequency is dominant over the entire pass-by, this frequency belongs to rank 1 for 100 % of the time, and so on.

This analysis shows that in the three passages of the same vehicle (a) the 404–707 Hz and the 1760–2825 Hz bands are always the most critical squealing bands. The total noise emission is dominated by the 404–707 Hz band for 74.2 %, 48 % and 46.8 % of the total time. While the 1760–2825 Hz band dominates the noise emission for the 28.8 %, 52 % and 52.1%. The 1130–1760 Hz becomes dominant only for 1.1 % of the whole curve negotiation of the third passage of vehicle (a). This confirms that the pattern observed for vehicle (a) once, is persistent on other passages of the same vehicle.

Looking at vehicles (b) and (c), the 404–707 Hz frequency interval is never found to be a dominant band concerning noise emission. Furthermore, the 1130–1760 Hz band is found to be the dominant for the 57.1 % and 56.7 % during the curve negotiation of vehicle (b) and (c) while the 1760–2825 Hz band dominates the noise emission for the 42.9 % and 39.1 % of the time. Noise contribution is dominated by the 3530–4400 Hz band for the 4.2 % of the time during the passage of vehicle (b). This confirms that, although vehicle (b) was measured only once, other vehicles of the same type present the same squealing behaviour.

To understand the reasons behind these dissimilar results, further investigations have been performed on the measurements associated to one of the passages of vehicle (a) and the passage of vehicle (b).

Spectrograms of the measured noise levels for the two different runs are presented in Fig. 2.

While noise peaks are mainly concentrated around 550 Hz and 2500 Hz in the first case (Fig. 2a), in the second one (Fig. 2b) the first squealing frequency detected is in the range 1200–1500 Hz. Different conditions of the wheel profiles, due to wear, may explain how vehicles with the same architecture and the same (nominal) wheel profiles generate noise at different squealing frequencies. The spectrogram of case (b) reveals also that the squealing frequencies occur in a wider range than case (a), where the tonal nature of the noise is more evident.

Squeal is taking place at frequency different from the wheel resonances, and this is visible in terms of a shift and a spread in the squealing frequencies (see Fig. 2b). This may be an indication that several modes are involved in the instability and therefore mode coupling can occur. It is possible that the eigenfrequencies of the wheels of tramcar (a) and tramcar (b) were different due to different wearing conditions. However, a change in the eigenfrequencies due to wear cannot justify the different vibration modes that were found to be excited during curve negotiation, as well as the presence of a shift and a spread in the squealing frequencies during the passage of tramcar (b) only.

In addition, the maximum noise level measured in case (b), (108 dBA) is found to be 6 dB higher than the one observed in case (a), (102 dBA).

The microphone signals were also processed by applying the fast time-weighting (see [24]). Fig. 3 shows the overall noise levels together with the contributions from specific frequency bands.

The analysis shows that the overall noise emission generated by tramcar (a) and tramcar (b) is always dominated by one frequency band at a time. The noise from tramcar (a) is characterized by noise emissions either in the bands centred at 500/630 Hz or at 2000/2500 Hz, while the overall noise emission from tramcar (b) is mostly dominated by the bands centred at 1250/1600 Hz with some smaller contributions from the bands at 2000/2500 Hz.

During the passage of the vehicle, the microphone is sensitive to the noise radiated by all the wheels of the tram (4 bogies). It was not possible to separate the contribution of the different wheels, nor it was possible to identify the squealing wheels at a given time. However, the spectrograms of the inner rail acceleration (see Fig. 4) suggest that most of the noise recorded by the microphone (Fig. 2) is generated by the inner wheels of the vehicle. In fact, the tonal frequencies highlighted in Fig. 2a and b are also present in the spectrogram of rail acceleration during the passage of vehicle (a) and (b) (see Fig. 4a and b).

It is reasonable to assume that small differences in how each bogie negotiates the curve can result in different squealing frequencies. For tramcar (a) and in this specific section, the contact conditions seem always to lead to squeal in the 500/630 Hz or 2000/2500 Hz frequency bands. On the other hand, when tramcar (b) runs over the same section of the line, the most frequent squealing frequency is contained in the bands centred at 1250/1600 Hz. For reasons that these results alone cannot yet clarify, the contact conditions associated with the different tramcars favour different squealing frequencies.

In addition, while the noise levels generated by the two tramcars at around 2500 Hz are similar (about 100 dBA), a noticeable increase is observed when the sound emission switches to the 1250/1600 Hz bands, reaching up to 108 dBA.

To investigate further the relation between the wheel/rail contact conditions and the squealing frequencies, the fast time-weighting SPL is compared in Fig. 5 with the signal measured by the accelerometer installed on the left check rail (the one on the inner side of the curve). The acceleration levels are processed using the same fast time-weighting and are presented with a reference value of 10^{-6} m/s^2. Both signals are A-weighted. Acceleration levels are reported on the left-hand y-axis (black continuous line) while the overall SPL is indicated on the right-hand axis. The acceleration levels allow identification of the passage of the four bogies over the instrumented section (identified with Roman numbers I-IV). Looking at case (a), sharp peaks are associated with the passage of each of the rear inner wheels of the bogies, which are in flange contact because of the very sharp curve radius (this is confirmed

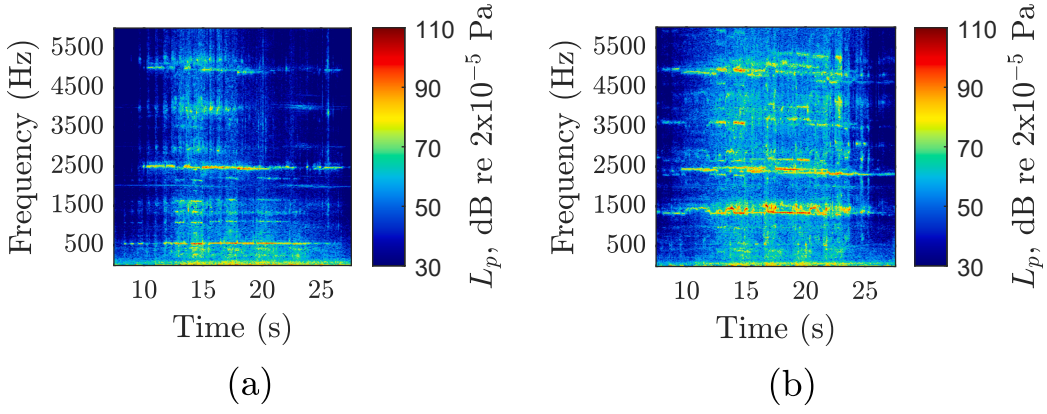

Fig. 2. SPL spectrograms (inner side of the curve, 2.5 m from the track centre) generated by: (a) tramcar a, and (b) tramcar b.

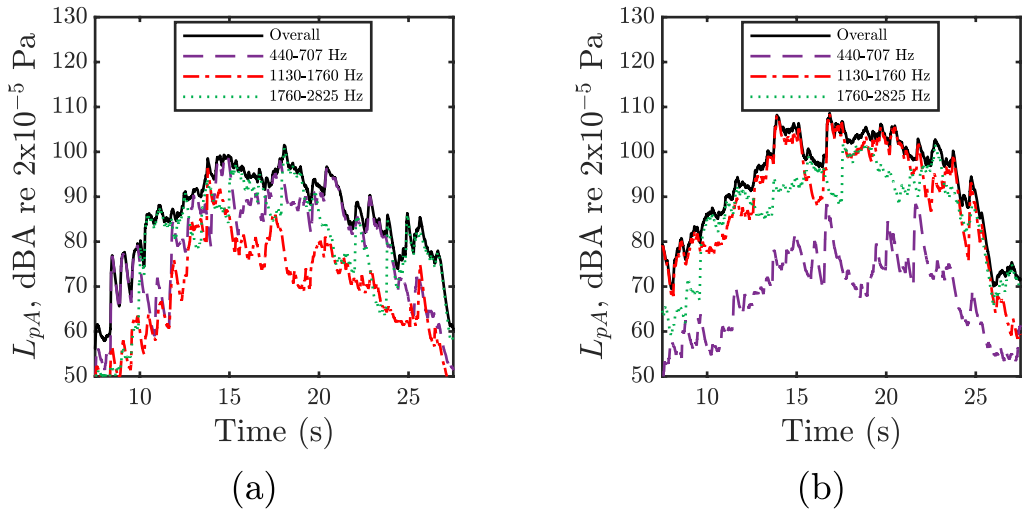

Fig. 3. Fast time-weighting SPL (inner side of the curve, 2.5 m from the track centre) generated by: (a) tramcar a, and (b) tramcar b.

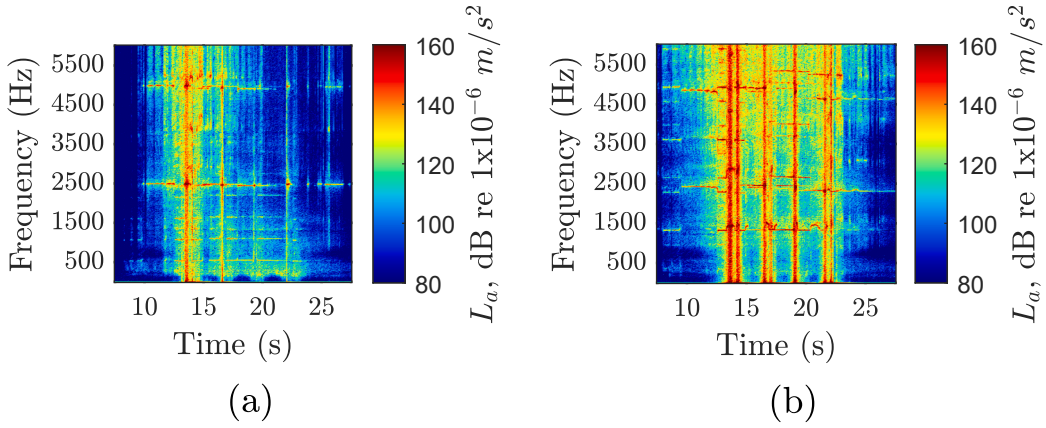

Fig. 4. Spectrograms of the inner rail lateral accelerations generated by: (a) tramcar a, and (b) tramcar b.

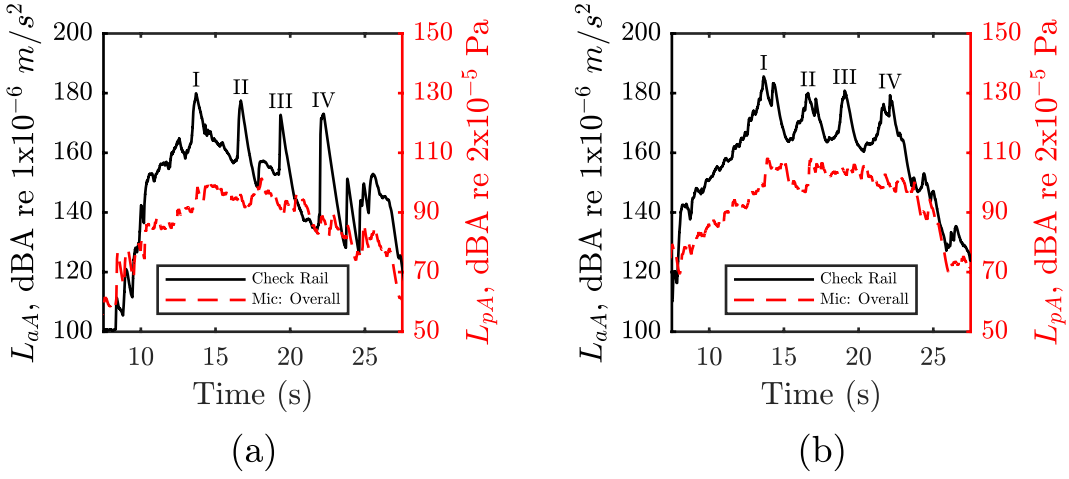

Fig. 5. Fast time-weighting SPL (inner side of the curve, 2.5 m from the track centre) and rail lateral accelerations generated by: (a) tramcar a, and (b) tramcar b.

by vehicle dynamics simulation, see Section 3 below). The contacts between the flange and the side of the rail head result in a strong lateral vibration that is also measured by the accelerometer placed on the check rail. The trend of the acceleration levels is slightly different for tramcar (b); in this case there are two peaks associated with the passage of bogies I, II and IV. The time delay between them (0.6 s) corresponds to the passage of the wheelbase (1.7 m) at 10 km/h. This implies that, in addition to the flange contact between the rear inner wheel of the bogie and the rail head, also a flange back contact between the front inner wheel and the check rail occurs. The presence of this second contact point for case (b) is believed to be the reason for the different squealing frequencies highlighted for the two tramcars.

The critical role of check rail contact on curve squeal was also observed by other authors [2,7], who measured severe noise levels up to 20 dB greater than the ones usually found in literature. In that case it was identified that the squeal occurred at the leading inner wheel and was associated with radial modes with 2–5 nodal diameters (2.2–4.5 kHz). These investigations confirm that the possible presence of multiple contact points should be considered to obtain more realistic curve squeal predictions.

To explore the effect of such contact conditions, a frequency-domain model that accounts for the presence of both single and multiple contact patches is presented in the following sections. This is then used to recreate the contact conditions of the measurements described in this section and to verify if the numerical results confirm the experimental observations at least in terms of a correspondence between the contact conditions and the squealing frequencies.

3. Vehicle dynamics simulation

A multibody model is adopted to describe the vehicle dynamics during curve negotiation. In this Section, the description of the reference tramcar analysed in the present study is provided and some results of the vehicle dynamics simulation in terms of wheel/rail contact forces on the leading bogie are presented.

The tramcar model is developed in an in-house vehicle dynamics software [25–27]. The mathematical model has been designed to reproduce the dynamics of the whole tramcar during curve negotiation. The carbodies are rigid in the model and are interconnected by kinematic constraints and/or elastic and viscous elements, replicating the actual connections between them. Large displacements and consequent kinematic non-linearities are considered. The equations of motion of the tramcar are formulated in terms of generalized coordinates that correspond to rigid body motions and mode shapes of each module component. The model has been validated against experimental data in [28].

The wheel/rail contact model is based on a multi-Hertzian approach [29,30] that enables the possibility of multiple simultaneous contact points. The multibody model allows to collect the steady state value of the virtual penetration between the wheel and the rail for each contact point. The linearized Hertzian contact stiffness can be then computed knowing the steady state normal load acting on the different contact points as proposed in [2,31]. Pre-calculated contact tables are used to store the results of the geometrical analysis of wheel and rail profiles to reduce the computational effort required during the simulation. The effect of the rubber elements interposed between the tyre and the web in the resilient wheels is included through a truncated modal approach. The importance of modelling accurately the actual wheel/rail contact condition when dealing with curve squeal prediction will be also shown in Section 6. The model is set up to replicate the negotiation of the curve under investigation during the experimental campaign. This is a 24 m radius left-hand curve. In the simulations the tramcar first runs in a straight line for 21 m, then it negotiates the curve for 51 m and finally

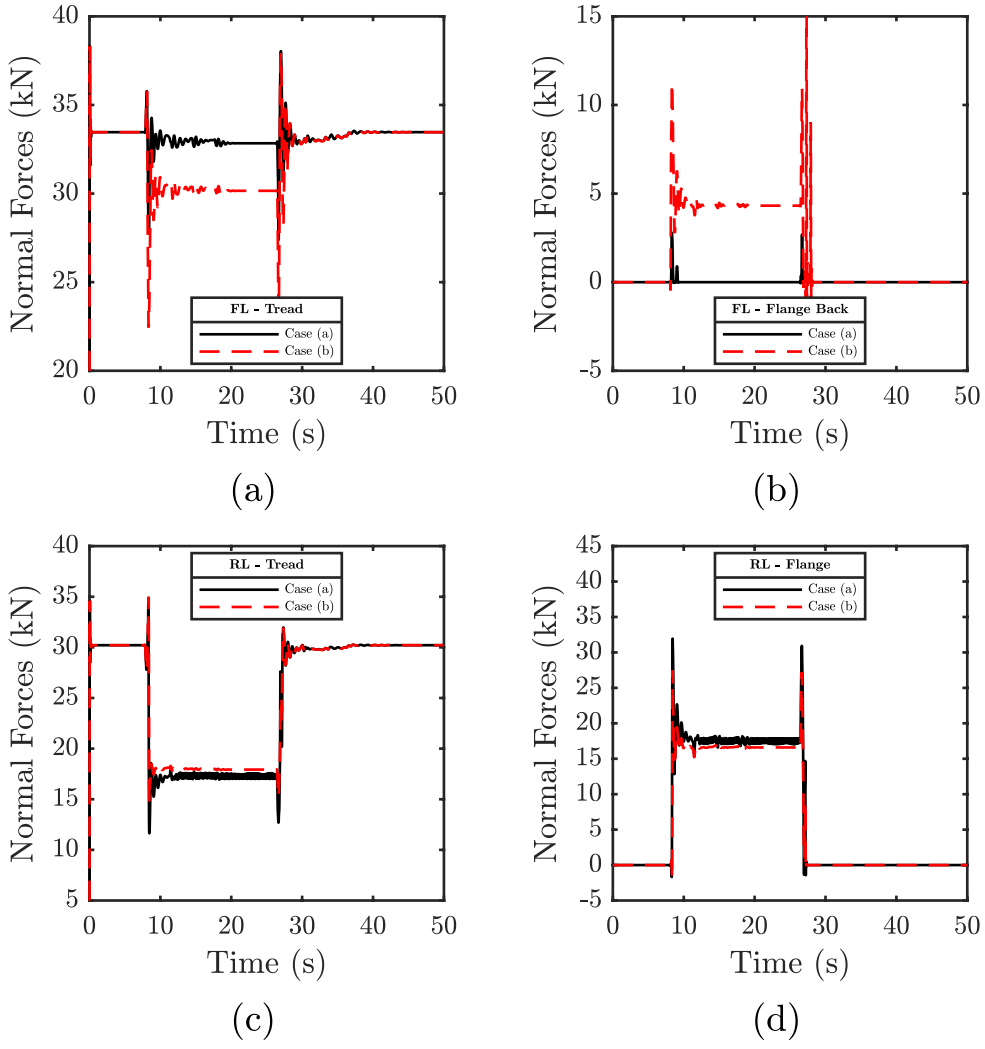

Fig. 6. Wheel/rail contact forces in normal direction: (a) Front Left, tread, (b) Front Left, flange back, (c) Rear Left, tread, (d) Rear Left, flange.

returns to a straight track. The speed in the simulation is set to 10 km/h, corresponding to the nominal speed in the tests.

Two simulation conditions are considered that correspond to either a single contact point condition (assumed in case a) or a multiple one (assumed in case b). The analysis is limited to the first bogie of the tramcar, being the inner leading wheel of the vehicle usually identified as the most critical concerning curve squeal occurrence, due to the high angle of attack between wheel and rail [2]. Similar wheel/rail contact conditions can be found also on the leading inner wheels of the other carbodies. The experimental evidence presented in Section 2 refers to two tramcars with the same architecture running on the same reference curve. Although it is plausible to assume that the different contact conditions are due to different wear condition of the wheels, the actual shapes of the profiles are unknown and cannot be used in the simulations. The contact between the wheel flange back and the check rail is instead induced by a modification in the rail gauge, which is increased from 1445 mm (standard rail gauge in the reference curve) to 1447 mm. Wheel/rail normal contact forces on the front and rear inner wheels of the bogie (left wheels) are analysed in some detail to verify that wheel/rail contact conditions simulated in case (a) and case (b) can be considered representative of the actual wheel/rail contact conditions during measurements. Normal forces acting on the tread, flange and flange back on the front left (FL) and rear left (RL) wheels are thus reported in Fig. 6. The main difference between case (a) and case (b) can be observed in Fig. 6b depicting the normal force on the wheel flange back. In fact, while in the case (a) the flange back contact at steady state is absent, a constant load of 4.3 kN is highlighted in case (b) simulation. The other flange-type contact observed is the one on the rear left wheel that is almost the same for case (a) and case (b). The presence of the flange contact only on the rear inner wheel (Fig. 6d, case (a) simulation) seems to be coherent with the isolated peaks highlighted in the check rail vibration measurements (Fig. 4a). Furthermore, a contact on the flange-back of the leading inner wheel (Fig. 6b, case (b) simulation) followed by a contact on the flange of the inner rear wheel (Fig. 6d, case (b) simulation) suggests the simulated scenario may be close to what highlighted in the check rail vibration measurements of case (b), where two successive peaks were found during the passage of bogie I,II,IV (Fig. 5b).

The results of the simulations are also presented in terms of lateral contact forces on the Front Left (FL), Rear Left (RL), Front Right (FR) and Rear Right (RR) wheels of the leading car with a focus on the steady-state normal and transverse contact forces acting on the leading inner wheel after 25 s. The word “lateral” refers to a reference system where the longitudinal axis is tangent to the track centreline while the word “transverse” refers to a local reference system tangent to the contact plane.

The first simulation (case (a)) is presented in Fig. 7. On this sharp curve both the front outer and the rear inner wheels of the first car are in flange contact. On the leading inner wheel (see Fig. 7b) the wheel/rail contact point is located on the wheel tread. As described in the previous paragraph looking at Fig. 6, this wheel/rail contact condition is assumed to be representative of the actual contact condition present during the measurement reported in Fig. 2a.

At the curve entrance (approximately 8 s in Fig. 7a) the leading axle moves from a centred position towards the right, until the maximum clearance is taken up and flange contact on the outer wheel takes place. Peaks in the lateral contact forces are observed due to the transition from a straight track to a curved one. Afterwards, the leading outer wheel pushes against the rail and moves along the curve in flange contact. As the curve is very sharp, due to the counter steering behaviour of the first bogie during curve negotiation, the rear axle moves towards the left with respect to the track centre line, resulting in flange contact on the rear inner wheel. When the wheel comes into flange contact, the sharp peaks in the wheel/rail lateral contact forces are generated on the front outer and rear inner wheels. After the transient, a steady-state curving condition is reached at about 15 s. Similar wheel/rail contact force oscillations occur when leaving the curve, when the front and rear wheelsets progressively return to a centred position with respect to the track.

In the second simulation (case (b), shown in Fig. 8), in which a 1447 mm rail gauge is introduced, a secondary contact occurs between the flange back and the check rail for the leading inner wheel, as shown in Fig. 8b.

This situation is assumed to be representative for the wheel/rail contact condition in Fig. 5b, in which double peak corresponding respectively to the flange back contact of the front inner wheel and the flange contact of the rear inner wheels is highlighted. The comparison between the results of cases (a) (Fig. 7) and (b) (Fig. 8) highlights that, while steady-state transverse creep forces in the tread contact patch are similar (11.8 kN in case (a) and 10.8 kN in case (b)), the total lateral force acting on the front left wheel is lower in case (b) (8.4 kN) than in case a (13.2 kN), due to the presence of the normal force acting on the flange back.

From this model, steady-state parameters, such as creepages, contact angle, normal load and contact stiffness, are identified at 25 s in both situations and are used as the input to the curve squeal prediction model.

4. Wheel/rail coupled model

The curve squeal prediction model adopted in this work is based on the theoretical model in the frequency domain proposed by Huang [9] and extended by Squicciarini et al. [10] to include the simultaneous presence of multiple contact points between wheel and rail. The possibility of curve squeal occurrence is predicted in two steps, with a simulation of vehicle dynamics in the time domain followed by a

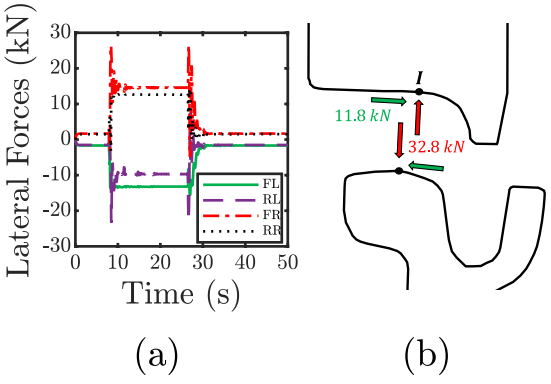

Fig. 7. Case a: (a) lateral wheel/rail contact forces on the first car of the vehicle, and (b) steady-state normal and transverse contact forces ($t = 25$ s) on the leading inner wheel.

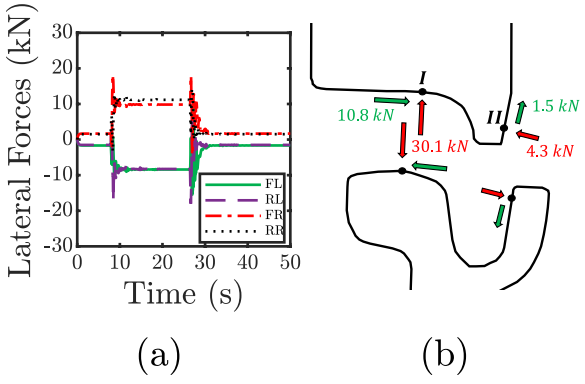

Fig. 8. Case b: (a) lateral wheel/rail contact forces on the first car of the vehicle, and (b) steady state normal and transverse contact forces (t = 25 s) on the leading inner wheel.

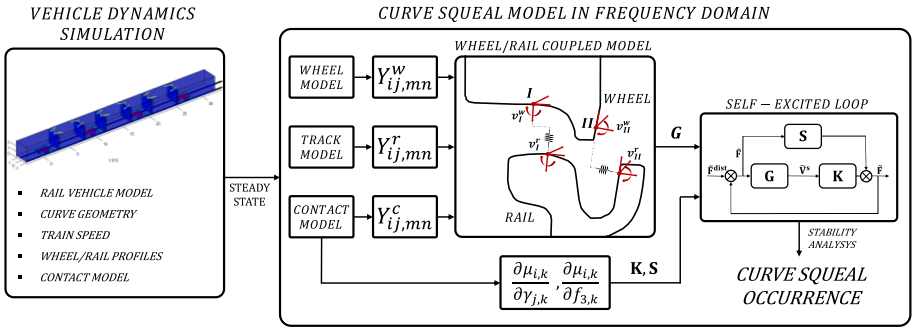

Fig. 9. Overview of the modelling approach: curve squeal occurrence is predicted by performing the stability analysis of the wheel/rail coupled system [2].

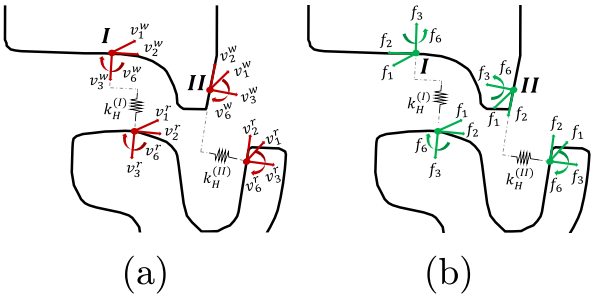

Fig. 10. Wheel/rail model conventions: (a) velocities, and (b) contact forces.

stability analysis of the wheel/rail coupled system in the frequency domain (see Fig. 9).

The wheel/rail interaction is described by means of a point-contact model, in which the wheel and the rail are coupled by contact forces incorporating a Hertzian spring in the normal direction [2,9]. The non-linear equations of motion describing the wheel/rail sliding velocities in the tangential directions are first presented in a time-domain formulation and then linearised about the steady-state curving condition defined in the multibody simulation. The wheel/rail dynamic behaviour is described considering the displacements in the longitudinal, transverse and normal directions and the spin rotation. Fig. 10 shows the sign convention adopted for wheel and rail velocities (Fig. 10a) and contact forces (Fig. 10b).

4.1. Single contact point formulation

The dynamic components of the contact forces, i.e. the fluctuations about their steady-state values, can be represented in a vector form:

$$\mathbf{f} = \begin{bmatrix} f_1 & f_2 & f_3 & f_6 \end{bmatrix}^T \tag{1}$$

and the dynamic fluctuations of the wheel and rail velocities are:

$$\mathbf{v^w} = \begin{bmatrix} v_1^w & v_2^w & v_3^w & v_6^w \end{bmatrix}^T \tag{2}$$

$$\mathbf{v^r} = \begin{bmatrix} v_1^r & v_2^r & v_3^r & v_6^r \end{bmatrix}^T \tag{3}$$

The local behaviour of the two contacting bodies is described by means of a Hertzian contact spring and its deformation, positive under compression, is expressed by:

$$d_3^c = -\left(d_3^r - d_3^w\right) = -\int_0^t \left(v_3^r - v_3^w\right) dt \tag{4}$$

To guarantee that contact is maintained, the overall sliding velocity in the normal direction must be equal to zero:

$$v_3^s = v_3^r - v_3^w + v_3^c = 0 \tag{5}$$

while in the longitudinal and transverse directions, as well as around the normal axis, non-zero dynamic sliding velocities exist and can be expressed as:

$$\begin{bmatrix} v_1^s \\ v_2^s \\ v_3^s \\ v_6^s \end{bmatrix} = \begin{bmatrix} v_1^r \\ v_2^r \\ v_3^r \\ v_6^r \end{bmatrix} - \begin{bmatrix} v_1^w \\ v_2^w \\ v_3^w \\ v_6^w \end{bmatrix} + \begin{bmatrix} v_1^c \\ v_2^c \\ v_3^c \\ 0 \end{bmatrix} \tag{6}$$

Creepages can be obtained as the sum of steady-state and dynamic components:

$$\begin{bmatrix} \gamma_{1tot} \\ \gamma_{2tot} \\ \gamma_{6tot} \end{bmatrix} = \frac{1}{v_0} \begin{bmatrix} v_{1tot}^s \\ v_{2tot}^s \\ v_{6tot}^s \end{bmatrix} = \frac{1}{v_0} \begin{bmatrix} v_{10}^s + v_1^s \\ v_{20}^s + v_2^s \\ v_{60}^s + v_6^s \end{bmatrix} = \begin{bmatrix} \gamma_{10} + \dfrac{v_1^s}{v_0} \\ \gamma_{20} + \dfrac{v_2^s}{v_0} \\ \gamma_{60} + \dfrac{v_6^s}{v_0} \end{bmatrix} \tag{7}$$

where v_0 is the reference vehicle speed along the curve.

The longitudinal and transverse forces together with the spin moment can be written as the product between the friction coefficient μ in i-direction (that is the creep force normalised against the normal load) and the normal contact force:

$$\begin{bmatrix} f_{1tot} \\ f_{2tot} \\ f_{6tot} \end{bmatrix} = \begin{bmatrix} \mu_1\left(\gamma_{1tot}, \gamma_{2tot}, \gamma_{6tot}, f_{3tot}\right) \\ \mu_2\left(\gamma_{1tot}, \gamma_{2tot}, \gamma_{6tot}, f_{3tot}\right) \\ \mu_6\left(\gamma_{1tot}, \gamma_{2tot}, \gamma_{6tot}, f_{3tot}\right) \end{bmatrix} f_{3tot} \tag{8}$$

where μ_1, μ_2, μ_6 are non-linear functions of the creepages and normal contact force ($f_{3tot} = f_{30} + f_3$). As the steady-state components of the friction forces are balanced by the forces exerted by vehicle suspension during curve negotiation, only the dynamic components are related to squeal:

$$\begin{bmatrix} f_1 \\ f_2 \\ f_6 \end{bmatrix} = \begin{bmatrix} f_{1tot} \\ f_{2tot} \\ f_{6tot} \end{bmatrix} - \begin{bmatrix} f_{10} \\ f_{20} \\ f_{60} \end{bmatrix} = \\ = \begin{bmatrix} \mu_1\left(\gamma_{1tot}, \gamma_{2tot}, \gamma_{6tot}, f_{3tot}\right) \\ \mu_2\left(\gamma_{1tot}, \gamma_{2tot}, \gamma_{6tot}, f_{3tot}\right) \\ \mu_6\left(\gamma_{1tot}, \gamma_{2tot}, \gamma_{6tot}, f_{3tot}\right) \end{bmatrix} (f_{30} + f_3) - \begin{bmatrix} \mu_1\left(\gamma_{10}, \gamma_{20}, \gamma_{60}, f_{30}\right) \\ \mu_2\left(\gamma_{10}, \gamma_{20}\gamma_{60}, f_{30}\right) \\ \mu_6\left(\gamma_{10}, \gamma_{20}, \gamma_{60}, f_{30}\right) \end{bmatrix} f_{30}. \tag{9}$$

It is possible to linearise Eq. (9) about a generic steady state curving condition, obtaining:

$$\begin{bmatrix} f_1 \\ f_2 \\ f_6 \end{bmatrix} = \frac{f_{30}}{v_0} \begin{bmatrix} \frac{\partial \mu_1}{\partial \gamma_1} & \frac{\partial \mu_1}{\partial \gamma_2} & \frac{\partial \mu_1}{\partial \gamma_6} & \frac{\partial \mu_1}{\partial f_3} \\ \frac{\partial \mu_2}{\partial \gamma_1} & \frac{\partial \mu_2}{\partial \gamma_2} & \frac{\partial \mu_2}{\partial \gamma_6} & \frac{\partial \mu_2}{\partial f_3} \\ \frac{\partial \mu_6}{\partial \gamma_1} & \frac{\partial \mu_6}{\partial \gamma_2} & \frac{\partial \mu_6}{\partial \gamma_6} & \frac{\partial \mu_6}{\partial f_3} \end{bmatrix} \begin{bmatrix} v_1^s \\ v_2^s \\ v_6^s \\ v_0 f_3 \end{bmatrix} + \begin{bmatrix} \mu_1 \\ \mu_2 \\ \mu_6 \end{bmatrix} f_3 \tag{10}$$

Assuming harmonic oscillations of the forces and the velocities (at the generic circular frequency ω), it is possible to move to the frequency domain:

$$f_i = F_i e^{j\omega t},\ v_i^r = V_i^r e^{j\omega t},\ v_i^w = V_i^w e^{j\omega t},\ v_i^c = V_i^c e^{j\omega t},\ v_i^s = V_i^s e^{j\omega t} \quad i = 1,2,3,6 \tag{11}$$

where F_i, V_i^r, V_i^w, V_i^c and V_i^s denote the complex amplitudes of the respective quantity at the given circular frequency ω. Thus, Eq. (6), becomes:

$$\mathbf{V^s} = \begin{bmatrix} V_1^s \\ V_2^s \\ V_3^s \\ V_6^s \end{bmatrix} = \begin{bmatrix} V_1^r \\ V_2^r \\ V_3^r \\ V_6^r \end{bmatrix} - \begin{bmatrix} V_1^w \\ V_2^w \\ V_3^w \\ V_6^w \end{bmatrix} + \begin{bmatrix} V_1^c \\ V_2^c \\ V_3^c \\ 0 \end{bmatrix} \tag{12}$$

The dynamic components of the sliding velocities can be written as the product between the vector of the dynamic contact forces and the coupled system mobility:

$$\mathbf{V^s} = \begin{bmatrix} V_1^s \\ V_2^s \\ V_3^s \\ V_6^s \end{bmatrix} = \begin{bmatrix} Y_{11} & Y_{12} & Y_{13} & Y_{16} \\ Y_{21} & Y_{22} & Y_{23} & Y_{26} \\ Y_{31} & Y_{32} & Y_{33} & Y_{36} \\ Y_{61} & Y_{62} & Y_{63} & Y_{66} \end{bmatrix} \begin{bmatrix} F_1 \\ F_2 \\ F_3 \\ F_6 \end{bmatrix} = \mathbf{YF} \tag{13}$$

where $Y_{ij} = Y_{ij}^r + Y_{ij}^w + Y_{ij}^c$ is the sum of the rail, wheel and contact mobilities (see Section 5). The latter is derived from the contact spring, which for the normal direction is defined through the linearized contact stiffness k_H [2,31]:

$$Y_{33}^c = \frac{j\omega}{k_H} \tag{14}$$

The transverse contact stiffness can be computed from the linearized Hertzian normal contact stiffness value, by adopting the following formula [32]:

$$\frac{1}{k_i} = \frac{\chi}{k_H} \quad i = 1,2 \tag{15}$$

χ is a value between about 1 and 1.4 that mainly depends on contact patch geometry:

$$\chi \approx 1 + \frac{\nu}{1-\nu}\left(\frac{1}{4} + \frac{1}{\pi}\tan^{-1} g\right) \tag{16}$$

where ν is the Poisson's ratio and g is equal to a/b for the stiffness in the longitudinal direction or b/a for the transverse one, in which a and b are the contact patch semi-axis lengths in longitudinal and transverse directions respectively [2,16]. Therefore, the mobility of the contact spring in the tangential direction can be computed as:

$$Y_{ii}^c = \frac{j\omega}{k_i} \quad i = 1,2 \tag{17}$$

Only the diagonal terms are included in the formulation of the contact mobility matrix. Returning to Eq. (13), the sliding velocities are the result of the contribution of tangential contact forces and normal load fluctuations. They can be separated as follows:

$$\widetilde{\mathbf{V}}^{\mathbf{s}} = \begin{bmatrix} V_1^s \\ V_2^s \\ V_6^s \end{bmatrix} = \begin{bmatrix} Y_{11} & Y_{12} & Y_{16} \\ Y_{21} & Y_{22} & Y_{26} \\ Y_{61} & Y_{62} & Y_{66} \end{bmatrix} \begin{bmatrix} F_1 \\ F_2 \\ F_6 \end{bmatrix} + \begin{bmatrix} Y_{13} \\ Y_{23} \\ Y_{63} \end{bmatrix} F_3 = \widetilde{\mathbf{Y}}\widetilde{\mathbf{F}} + \mathbf{d}F_3 \tag{18}$$

where $\widetilde{\boldsymbol{Y}}$ is obtained removing the rows and the columns of the matrix $\boldsymbol{Y}$ related to the normal direction (3), as a consequence of Eq. (5):

$$\widetilde{\mathbf{Y}} = \mathbf{EYE}^T \tag{19}$$

where the matrix $[\boldsymbol{E}]$ is defined as:

$$\boldsymbol{E} = \begin{bmatrix} 1 & 0 & 0 & 0 \\ 0 & 1 & 0 & 0 \\ 0 & 0 & 0 & 1 \end{bmatrix} \tag{20}$$

Then, combining Eq. (5) and the third equation in the matrix of Eq. (13), yields:

$$F_3 = -\begin{bmatrix} \frac{Y_{31}}{Y_{33}} & \frac{Y_{32}}{Y_{33}} & \frac{Y_{36}}{Y_{33}} \end{bmatrix} \widetilde{\mathbf{F}} = \mathbf{b^T}\widetilde{\mathbf{F}} \tag{21}$$

and substituting Eq. (21) in Eq. (18):

$$\widetilde{\mathbf{V}}^{\mathbf{s}} = \left(\widetilde{\mathbf{Y}} + \mathbf{db^T}\right)\widetilde{\mathbf{F}} = \mathbf{G}\widetilde{\mathbf{F}} \tag{22}$$

The relationship between the tangential contact forces and the sliding velocities is given by the matrix of the wheel/rail coupled system $\boldsymbol{G}$. The relationship between contact forces and creepages (obtained by reformulating Eq. (10)) is introduced hereafter:

$$\widetilde{\mathbf{F}} = \begin{bmatrix} F_1 \\ F_2 \\ F_6 \end{bmatrix} = \mathbf{K} \begin{bmatrix} V_1^s \\ V_2^s \\ V_6^s \end{bmatrix} + \mathbf{R}F_3 \tag{23}$$

The matrix $\mathbf{K}$ represents the effect of the variation in the friction coefficient due to a fluctuation in the creepages and $\mathbf{R}$ represents the effect of a fluctuation in the normal load:

$$K_{ij} = \frac{f_{30}}{v_0}\frac{\partial \mu_i}{\partial \gamma_j}; \quad R_i = \mu_i + f_{30}\frac{\partial \mu_i}{\partial f_3} \tag{24}$$

In Eq. (24), f_{30} is the steady-state value of the normal load, μ_i is the friction coefficient in the i-direction, γ_j is the creepage in the j-direction and f_3 is the dynamic force in the normal direction. The friction coefficient is computed by introducing the heuristic formula derived from Kraft [33] proposed by Huang [9] into the Shen-Hedrick-Elkins theory [34] to include the effect of falling friction (Eq. (25)):

$$\mu(\gamma_{tot}) = \mu_0(1 - \lambda e^{-\tau/\gamma_{tot}}) \tag{25}$$

$$\gamma_{tot} = \sqrt{\gamma_1^2 + \gamma_2^2} \tag{26}$$

where the slope of the friction curve is defined by the falling ratio λ and the saturation coefficient τ, while μ_0 is the static friction coefficient and γ_{tot} in Eq. (26) is the total creepage. As an example, Fig. 11 shows the effect of varying the falling friction parameters λ and τ on the relation between normalised transverse friction force μ_2 and transverse creepage γ_2 (in the absence of other creep components). The value of μ_0 is 0.4 in both cases. The value of τ is 0.05 in Fig. 11a and the value of λ is 0.4 for Fig. 11b.

Combining Eq. (21), Eq. (22) and Eq. (23), the equation describing the self-excited loop, considering a single wheel/rail contact point, is obtained:

$$\widetilde{\mathbf{F}} = (\mathbf{KG} + \mathbf{Rb^T})\widetilde{\mathbf{F}} = (\mathbf{KG} + \mathbf{S})\widetilde{\mathbf{F}} \tag{27}$$

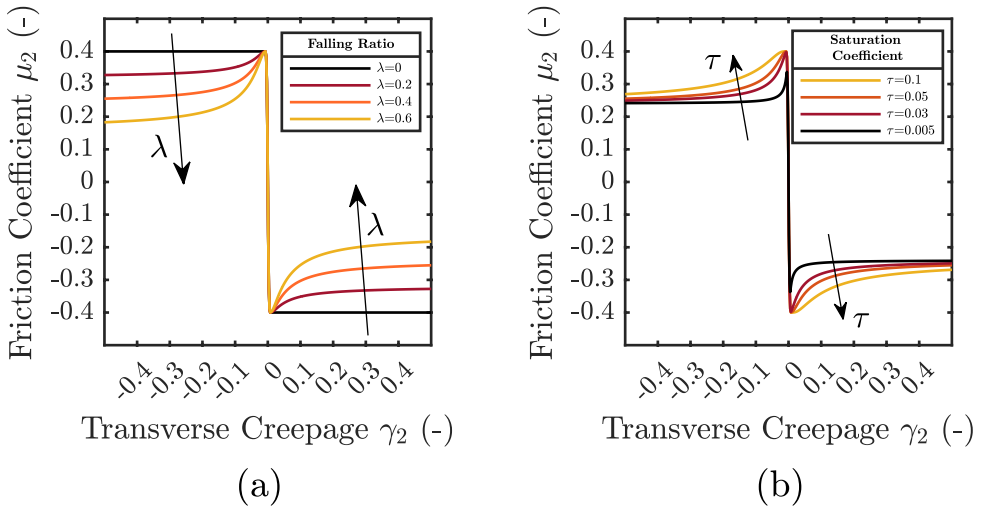

Fig. 11. Effects on friction curve of (a) falling ratio λ, and (b) saturation coefficient τ.

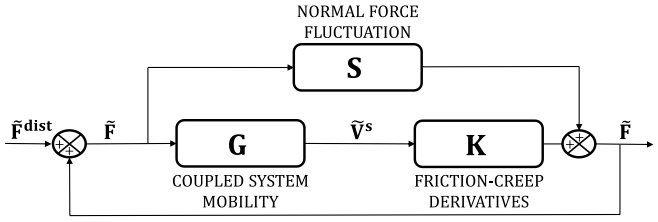

Fig. 12. Wheel/rail self-excited loop in the frequency domain. Instability can be introduced by a fluctuation in the contact forces as the result of a variation in creepages **K** and/or in normal load **S**.

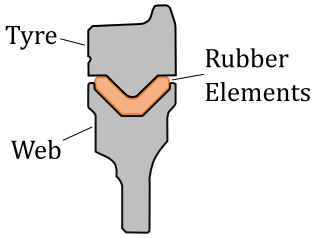

Fig. 13. Resilient wheel cross section.

Rearranging Eq. (27) it is possible to define the expression of the open-loop transfer function matrix $\boldsymbol{Q} = (\mathbf{KG} + \boldsymbol{S})$ of the Multi-Input Multi-Output (MIMO) system shown in Fig. 12. $\tilde{\mathbf{F}}^{dist}$ indicates a generic disturbance in the wheel/rail contact forces that can alter the steady state condition.

The stability analysis of the MIMO system about the steady-state curving condition is used to determine the behaviour of the wheel/rail coupled system at each frequency. The stability analysis is performed through the Nyquist Generalized Criterion for MIMO systems [35,36].

4.2. Multiple contact points formulation

The wheel/rail coupled model for a single contact point can be extended to include the presence of a second wheel/rail contact patch by reformulating Eq. (13) as

$$\boldsymbol{V}^s = \begin{bmatrix} \boldsymbol{V}_1^s \\ \boldsymbol{V}_2^s \end{bmatrix} = \begin{bmatrix} \mathbf{Y}_{11} & \mathbf{Y}_{12} \\ \mathbf{Y}_{21} & \mathbf{Y}_{22} \end{bmatrix} \begin{bmatrix} \mathbf{F}_1 \\ \mathbf{F}_2 \end{bmatrix} \tag{28}$$

where $\mathbf{Y_{mn}}$ is the system mobility matrix containing the point and transfer contributions of the $m,n = 1,2$ contact points. Thus, the generic term $Y_{ij,mn}$ consists of the sliding velocity of the m-th contact point in the i-th direction as the result of applying a unit dynamic force at the n-th contact point in the j-th direction.

Assuming the overall sliding velocities of the n-th contact point in the normal direction are zero (see Eq. (5)) it is possible to define the following quantities:

$$\mathbf{d}_\mathbf{n}^\mathbf{T} = \begin{bmatrix} Y_{13,1n} & Y_{23,1n} & Y_{63,1n} & Y_{13,2n} & Y_{23,2n} & Y_{63,2n} \end{bmatrix} \; n = 1,2 \tag{29}$$

$$\mathbf{a}_\mathbf{n}^\mathbf{T} = \begin{bmatrix} \frac{Y_{31,n1}}{Y_{33,nn}} & \frac{Y_{32,n1}}{Y_{33,nn}} & \frac{Y_{36,n1}}{Y_{33,nn}} & \frac{Y_{31,n2}}{Y_{33,nn}} & \frac{Y_{32,n2}}{Y_{33,nn}} & \frac{Y_{36,n2}}{Y_{33,nn}} \end{bmatrix} \; n = 1,2 \tag{30}$$

$$\mathbf{b}_\mathbf{n}^\mathbf{T} = \frac{Y_{33,11}Y_{33,22}}{Y_{33,11}Y_{33,22} - Y_{33,12}^2} \left(-\mathbf{a}_\mathbf{n}^\mathbf{T} + \frac{Y_{33,12}}{Y_{33,nn}} \mathbf{a}_{\mathbf{3-n}}^\mathbf{T} \right) \; n = 1,2 \tag{31}$$

Eq. (22) can now be reformulated to include the contribution of the second contact point:

$$\tilde{\mathbf{V}}^s = \begin{bmatrix} \tilde{\mathbf{V}}_1^s \\ \tilde{\mathbf{V}}_2^s \end{bmatrix} = \left(\tilde{\mathbf{Y}} + \mathbf{d_1} \mathbf{b}_1^\mathbf{T} + \mathbf{d_2} \mathbf{b}_2^\mathbf{T} \right) \begin{bmatrix} \tilde{\mathbf{F}}_1 \\ \tilde{\mathbf{F}}_2 \end{bmatrix} = \mathbf{G}\tilde{\mathbf{F}} \tag{32}$$

Combining Eq. (32) and Eq. (23), the equation describing the self-excited loop considering two wheel/rail contact points is obtained:

$$\begin{bmatrix} \tilde{\mathbf{F}}_1 \\ \tilde{\mathbf{F}}_2 \end{bmatrix} = \left(\begin{bmatrix} \mathbf{K}_1 & \mathbf{0} \\ \mathbf{0} & \mathbf{K}_2 \end{bmatrix} \mathbf{G} + \begin{bmatrix} \mathbf{R}_1 & \mathbf{0} \\ \mathbf{0} & \mathbf{R}_2 \end{bmatrix} \begin{bmatrix} \mathbf{b}_1^\mathbf{T} \\ \mathbf{b}_2^\mathbf{T} \end{bmatrix} \right) \begin{bmatrix} \tilde{\mathbf{F}}_1 \\ \tilde{\mathbf{F}}_2 \end{bmatrix} = (\mathbf{KG} + \mathbf{S}) \begin{bmatrix} \tilde{\mathbf{F}}_1 \\ \tilde{\mathbf{F}}_2 \end{bmatrix} \tag{33}$$

As the system mobility matrix **G** is a fully populated matrix, the systems of equations describing the wheel/rail dynamics at the two contact points are coupled. The stability analysis to predict curve squeal occurrence is performed by adopting the same approach adopted in the single contact point formulation [35,36].

Table 1
FE model parameters.

Parameter	Unit	Value
R_w	m	0.33
E_{steel}	MPa	210
ν_{steel}	–	0.3
E_{rubber}	MPa	36
ν_{rubber}	–	0.475

Table 2
Measured natural frequencies (f_n) and damping ratios (ξ_n) and predicted mode shapes (colormap refers to modal displacement magnitude) of the wheel modes with the highest curve squeal occurrence (ND = number of nodal diameters).

Mode No –	Mode Type –	Natural Frequency f_n, Hz	Damping Ratio ξ_n,%	Modeshape –
1	Axial-2ND	535	0.80	
2	Axial-3ND	1273	0.72	
3	Radial-3ND	1423	1.11	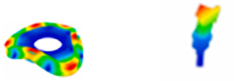
4	Web Axial-0ND	1560	0.45	
5	Radial-4ND	2230	0.49	
6	Axial-4ND	2479	0.38	
7	Tyre Torsion-1ND	2537	0.59	
8	Tyre Radial-0ND	2774	0.76	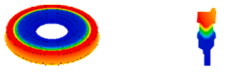
9	Radial-5ND	3367	0.58	
10	Axial-5ND	3736	0.77	
11	Axial-6ND	5112	0.53	

* As it is difficult to distinguish purely axial/radial modes (due to their strong coupling), the nomenclature is defined according to the direction of maximum vibration amplitude at the nominal contact point.

5. Wheel and rail mobilities

The Finite Element Method (FEM) is used to create a model of the resilient wheel in order to reproduce its structural dynamics, in particular to estimate its mobility at the wheel/rail contact points as required in the model.

The wheels of this tram have a nominal radius of 0.33 m and incorporate 24 V-shaped rubber elements positioned between the tyre and the web. A 3D model of the wheel has been developed adopting 159,378 brick elements. The rubber elements are modelled as an equivalent rubber ring assuming a linear elastic material. The wheel is clamped in the hub. The cross section of the wheel is shown in Fig. 13 and the FE model parameters are reported in Table 1. R_w is the wheel nominal radius while E_{steel}, E_{rubber} and ν_{steel}, ν_{rubber} are the Young modulus and the Poisson coefficients adopted to model steel and rubber components.

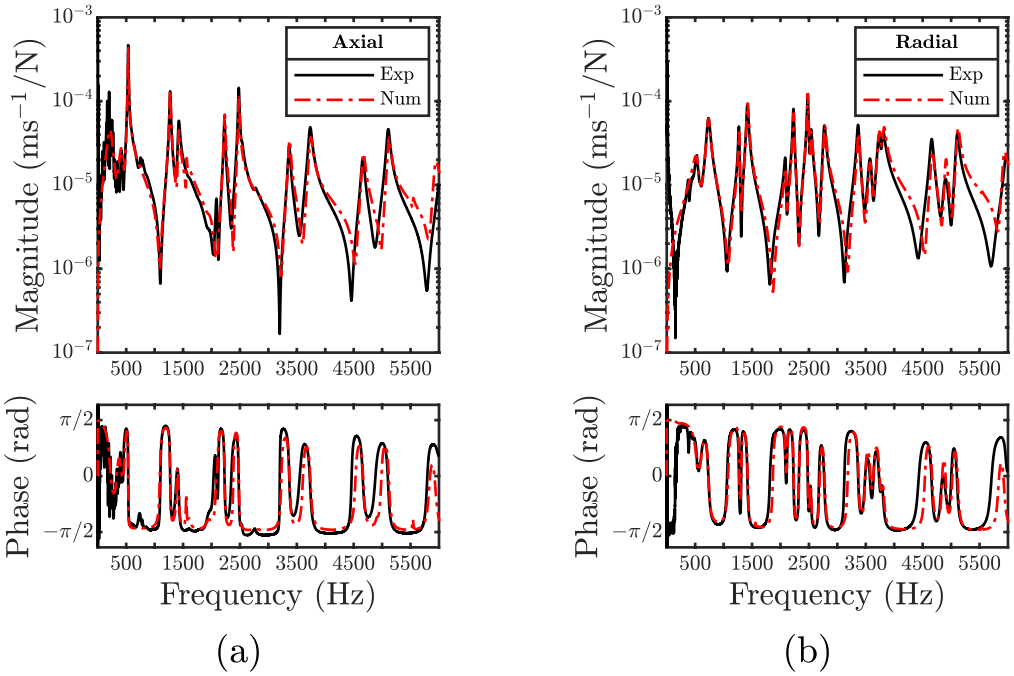

Fig. 14. Wheel mobility (a) in axial direction, and (b) in radial direction: comparison between experimental (—) and numerical results (- -).

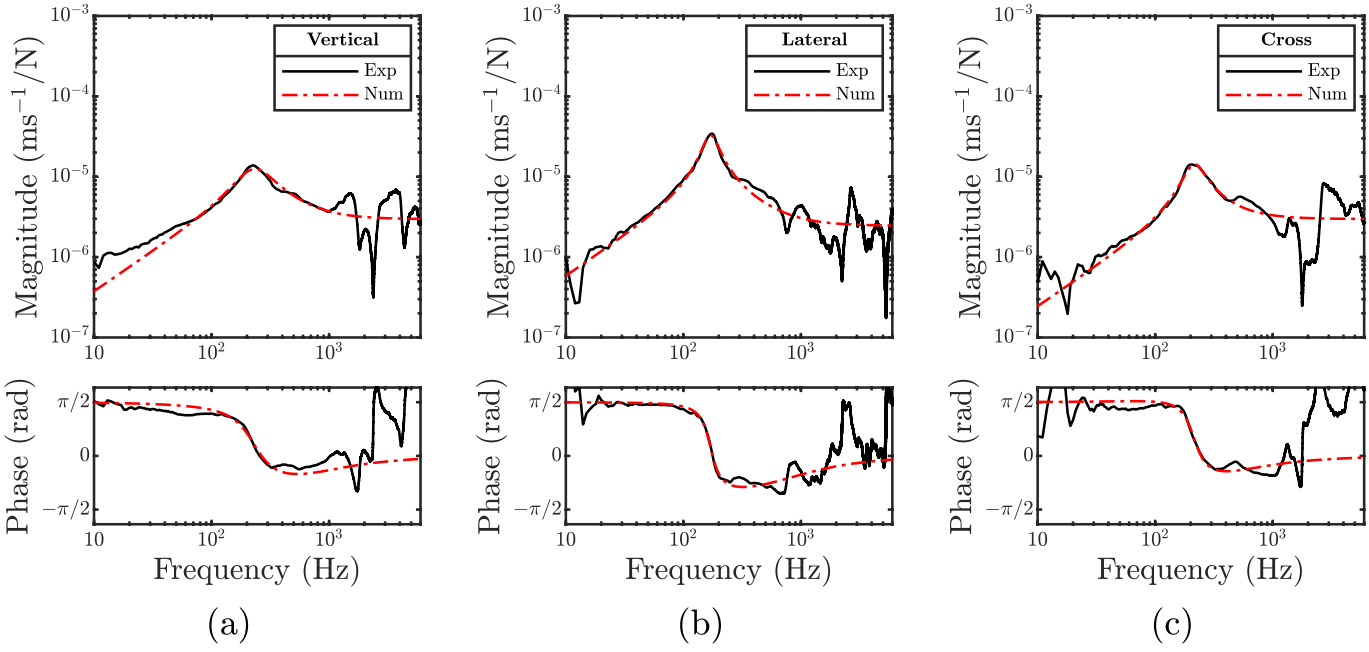

Fig. 15. Comparison between experimental (—) and numerical mobilities on rail head (- -): (a) vertical, (b) lateral, (c) vertical-lateral cross.

This wheel model was validated by means of a comparison with the results of an Experimental Modal Analysis (EMA) performed on a wheel of a similar tramcar to that used in the running tests. The wheel modes of vibration that are found to be the most relevant concerning curve squeal occurrence in the numerical simulations discussed in Section 6 are reported in Table 2, together with the measured natural frequency (f_n) and damping ratio (ξ_n).

The presence of a rubber layer between the wheel tyre and the web results in coupling between different directions so that modes that are predominately axial will also exhibit a significant component of vibration in the radial direction and vice versa. When two such modes have natural frequencies that are close to each other, an instability due to mode coupling may occur [5]. This is studied further in Section 6.

The modal superposition approach is used to compute the wheel point and transfer mobilities considering the longitudinal, lateral and vertical velocities and the spin rotation for each potential contact point (tread, flange back and flange)

$$Y^{w}_{ik}(\omega) = \sum_{n} \frac{j\omega\phi_{in}\phi_{kn}}{m_n\left(\omega_n^2 - \omega^2 + 2j\xi_n\omega_n\omega\right)} \quad i,k = 1,2,3,6 \tag{34}$$

where ω_n is the measured natural circular frequency of the mode n, ξ_n is the measured modal damping and m_n is the modal mass. The numerator includes the modal amplitudes ϕ_{in}, ϕ_{kn} (obtained from the FE model) associated with the n-th mode and the degrees of freedom i,k.

Table 3
Nominal parameter values and relative variation ranges (Δ) for curve squeal simulations of case (a) and case (b).

Parameter	Symbol (*Unit*)	Case (a)	Case (b)*		Δ
Vehicle Speed	v_0 ($km\ h^{-1}$)	10	10		±20 %
Normal Force	f_{30} (kN)	32.8	30.1	4.3	±20 %
Longitudinal Creepage	γ_{10} (−)	1e−5	−1e−3	9e−3	±20 %
Transverse Creepage	γ_{20} (−)	0.04	0.04	0.14	±20 %
Spin Creepage	γ_{60} (m^{-1})	−0.13	−0.13	2.93	±20 %
Contact Angle	θ (°)	2.5	2.6	−75.3	±20 %
Lateral CP Position**	Δl_2 (m)	[−0.005, 0.005]			–
Friction Coefficient	μ (−)	[0.2, 0.7]			–
Falling Ratio	λ (−)	[0, 0.2]			–
Saturation Coefficient	τ (−)	[0.01, 0.08]			–

*Tread CP (left column) and flange back CP (right column).
**CP: Contact Point.

A comparison between measured and predicted mobilities for the radial and axial direction on the wheel tread is presented in Fig. 14. A good correlation between numerical and experimental results is achieved up to 6 kHz, which is commonly the frequency range of interest concerning curve squeal noise phenomena [7].

The analysis carried out by Ding et al. [11] highlights the only significant effect of the rail dynamics on curve squeal prediction is found to be related to the "damping-like" behaviour of the rail at high frequency, which may lead to instability due to a "coupling-like" mechanisms between the wheel and the rail. Similar results were highlighted by Lai et al. in [12]. These findings suggest that a rather simple track model can be adopted to carry out curve squeal prediction, without the need of including rail cross-section deformation, pinned–pinned resonances, or effect of multiple wheels [11]. Therefore, the dynamic behaviour of the track is introduced in the wheel/rail interaction model by means of an equivalent system with a transfer function defined as the ratio of two polynomials:

$$H(s) = \frac{B(s)}{A(s)} = \frac{b_1 s^{m-1} + b_2 s^{m-2} + \ldots + b_m}{s^m + a_1 s^{m-1} + a_2 s^{m-2} + \ldots + a_m} \tag{35}$$

This approach has been used to reproduce the frequency response functions of the railway track [37,38] and is here applied to the Embedded Rail System (ERS) of this study. ERS frequency response functions are measured through impact tests, adopting an impact hammer to excite the track in the vertical and lateral directions. The track response is measured by a set of accelerometers mounted on the rail head and check rail. Point mobilities in the vertical and lateral directions, as well as transfer mobilities for rail head and check rail contact points, are computed and fitted to the on-site measurements. The results for the vertical, lateral and cross mobility are shown in Fig. 15. A filter of second order ($m = 2$) is chosen for the curve fitting procedure. The same procedure has been performed for the transfer mobilities between the two contact points (results not shown here). The magnitude of the vertical-lateral cross mobilities in this grooved rail system is high and comparable to the direct terms (Fig. 15c) and, on the other hand, the longitudinal dynamics of the track are neglected due to its high impedance in this direction. Similarly, also the spin mobility is not included in the current model.

The point and cross mobilities of the rail head estimated by the identified model are in good agreement up to 2 kHz with the experimental curves.

6. Prediction of curve squeal occurrence

The intermittent nature of curve squeal and the unpredictable variability of contact parameters suggest that a statistical approach is suitable to gain a better understanding of the problem. Thanks to the high computational efficiency of the frequency-domain formulation, it is possible to carry out a set of simulations accounting for a random variation of the most relevant input parameters of the model. This strategy was already adopted in [10]. Following the experimental observations highlighted in Section 2, a numerical assessment on the role of single and multiple contacts between wheel and rail is carried out in this section. A set of 100 simulations is considered for each situation. Vehicle and friction parameters are obtained for each of the 100 simulated cases by extracting random values from a uniform distribution. A ±20 % variation is applied to the vehicle speed and steady-state values of creepages, normal force and wheel/rail contact angle. A fluctuation in the lateral contact position, limited to ±5 mm, is obtained through a translation of the mobility matrix (see [16]). Intervals for parameter variation are also defined for the friction coefficient and falling friction parameters λ and τ. A wide range of variability is included in the value of friction coefficient to consider also the most critical scenarios for curve squeal occurrence. The interval is limited to the friction coefficient measured on dry rail in [39]. The intervals for falling friction parameters are defined around the values adopted in [5,9,16]. Prediction of curve squeal occurrence is carried out considering the leading inner wheel of the vehicle for both case (a) and case (b). The summary of the model parameters subjected to random variations and the variation ranges are presented in Table 3.

Falling friction and mode-coupling mechanisms are usually attributed as the cause of curve squeal events. In the first set of results presented below the two mechanisms are present together in the simulations. To explore the effect of mode coupling alone, the same simulations are then recalculated in the absence of falling friction.

6.1. Simulation with falling friction

Numerical predictions including falling friction for case (a) are presented in Fig. 16a. The results of curve squeal predictions are presented in terms of unstable frequencies which, for each simulation, are superimposed on the axial and radial mobilities of the wheel. The red dots indicate the presence of an instability in the wheel/rail coupled system at the corresponding frequency. For this case, curve squeal is expected at frequencies close to 535 Hz (axial mode, 2 ND), 1273–1423 Hz (axial and radial modes, 3 ND) and 2479 Hz (axial mode, 4 ND). A few unstable points are also predicted at about 3736 Hz (axial mode, 5 ND) and 5112 Hz (axial mode, 6 ND). The diagram allows an estimate to be made of the wheel vibration modes which are most prone to squeal, according to the number of the unstable occurrences within the total number of simulated variants. The set of simulations for case (a) suggests that it is very likely that squeal develops at frequencies close to the 2 ND and the 4 ND axial modes (535 Hz and 2479 Hz respectively). The occurrence of fewer unstable points in the frequency range 1200–1600 Hz means that the

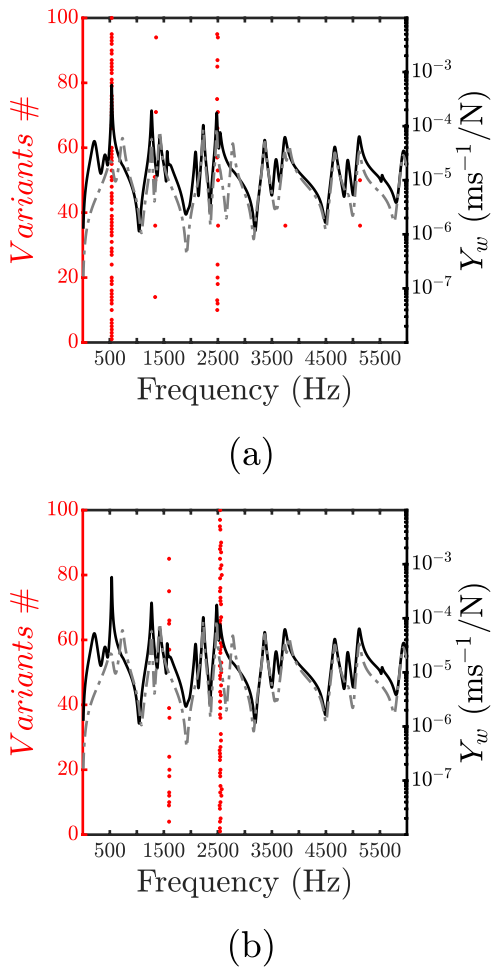

Fig. 16. Curve squeal simulation results for (a) single and (b) multiple contact points. Red dots (•) indicate system instabilities for each of the 100 simulated variants. Unstable points are depicted against wheel mobility in axial (—) and radial (- -) directions. (For interpretation of the references to colour in this figure legend, the reader is referred to the web version of this article.)

instability of the 3 ND axial and radial modes is less likely and arises only in the presence of specific wheel/rail contact conditions (further away from the steady-state parameters identified in the vehicle dynamics simulation) or only under critical friction conditions (high friction coefficient or strong falling friction effect).

The squealing frequencies predicted in the first analysis are in good agreement with the ones observed in the pass-by measurements on the first tramcar (see Fig. 2a), where the noise is dominated by the 550 Hz and 2500 Hz tonal contributions.

Numerical simulations of case (b) (see Fig. 16b) confirm that the presence of a flange back contact point alters the squealing frequencies involved. The system instability close to 535 Hz is completely suppressed in this case. To clarify this, Fig. 17 shows the mode shapes of the

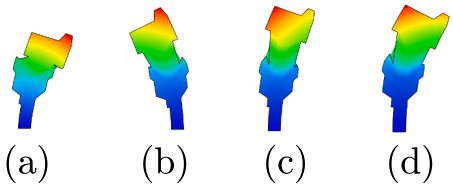

Fig. 17. Cross-section of unstable wheel axial and radial vibration modes predicted by numerical simulations: (a) axial 2 ND (535 Hz), (b) axial 3 ND (1273 Hz), (c) radial 3 ND (1423 Hz), (d) axial 4 ND (2479 Hz).

modes associated with the most common squealing frequencies. The wheel mode at 535 Hz is mostly axial and flange back contact is preventing its excitation for two reasons. First, the flange back contact is limiting the wheel/rail relative motion in the axial direction, preventing or at least decreasing the excitation of wheel modes where axial displacements are predominant. The contribution of this physical constraint is relevant at low frequency, where the contact mobility is limited. The lower total force in the lateral direction detected on the inner wheel of case b (Fig. 8a) compared with case (a) (Fig. 7a) is the second reason why the excitation of wheel modes with predominantly axial displacement is decreased.

The higher frequency 3–4 ND axial and radial modes, found to be unstable in both situations, have a significant modal component in both axial and radial directions (see Fig. 17b, 17c, 17d) meaning that a flange back contact is no longer limiting the instability associated with these modes. Furthermore, the tangential forces acting on the flange back have a significant component in the radial direction that can also promote their instability. Thus, a contact on the flange back, in the presence of a close pair of modes with significant axial and radial modal components (such as the pair of modes at 1273 and 1423 Hz, see Fig. 17b, and c) could favour a mode-coupling type instability.

In Fig. 16b, an increase in the instability occurrence is observed at about 1400–1600 Hz and 2400–2600 Hz. The squealing frequencies predicted in these frequency ranges seem to be shifted with respect to the ones obtained in Fig. 16a. Different unstable frequencies may occur due to different modes being involved in the two situations or, as stated above, due to mode-coupling phenomena, which usually arise when there are two vibration modes that are close in frequency. The large spread in the squealing frequencies observed in noise measurements of case (b) (see Fig. 2b) suggests a possible and intermittent mode-coupling mechanism was taking place, especially looking at the range 1200–1600 Hz (see also [5]). This mechanism may have been favoured by the presence of a second contact point on the flange back, which was promoting the exchange of energy between the axial and radial directions.

6.2. *Simulation without falling friction*

The curve squeal analysis is repeated by reproducing each of the 100 variants simulated in Section 6.1 (see Fig. 16) without falling friction, meaning that the only reason for instabilities is mode coupling. The absence of falling friction is modelled by assuming $\mu = \mu_0$ (see Eq. (25)) in the Shen Hedrick Elkins contact model. The results are shown in Fig. 18. While the results for case (b) are similar to the analysis with falling friction, no unstable points are obtained in the simulations for case (a). This confirms that the multiple wheel/rail contact condition may favour the development of mode-coupling mechanisms.

Because it is difficult to identify whether the system instability is due to a coupling of two or more modal contributions, the 100 variants for case (b) are repeated by removing one or more wheel vibration modes. The results of this analysis are summarised in Table 4. Each row of the table represents a squeal simulation of case (b) in which a wheel mode contribution is removed from the mobilities. The ranges of the unstable frequencies for each of the simulated cases are given in the third and fourth columns.

Instability in 1400–1600 Hz frequency range occurs only in the presence of the 3ND radial mode (1423 Hz). If this mode is removed, no unstable cases in that frequency range are obtained. Removing the wheel modes at 1273 Hz or 1560 Hz does not alter the unstable frequency obtained in the complete simulation (Fig. 16b). However, by removing both these wheel modes, no unstable cases are obtained, meaning that system instability arises only in the presence of a pair of wheel vibration modes that are close in frequency. Analyses are also performed by removing the wheel vibration modes at 2479, 2537 Hz and 2774 Hz and no noticeable change in the frequencies involved are observed apart from the case in which the 2479 Hz modal contribution is suppressed. Similar to the 1400–1600 Hz range, the wheel mode at

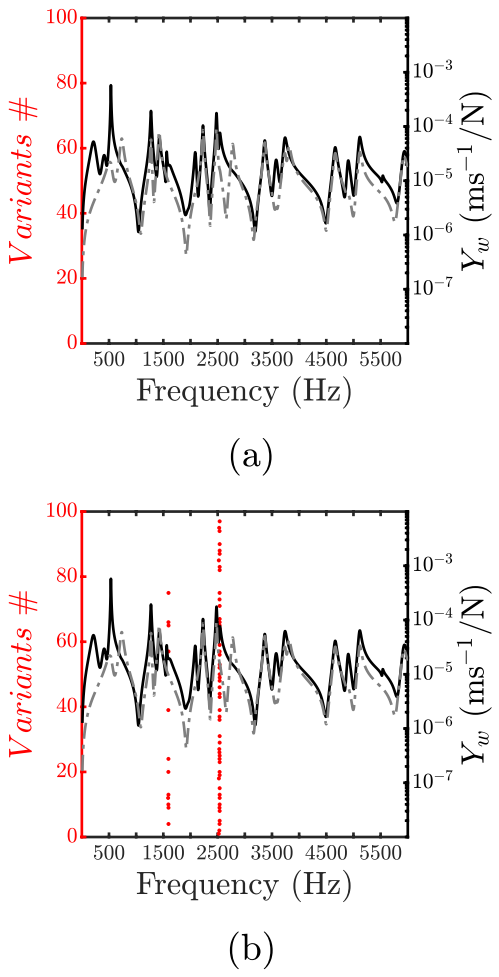

Fig. 18. Curve squeal simulation results for (a) single and (b) multiple contact points without falling friction effect. Red dots (•) indicate system instabilities for each of the 100 simulated cases. (For interpretation of the references to colour in this figure legend, the reader is referred to the web version of this article.)

2479 Hz alone is not capable of promoting instability without the presence of falling friction.

7. Conclusions

Curve squeal noise measurements on a modern low floor tramcar have revealed an important influence of the contact between the flange back of the leading inner wheel and the check rail on noise levels and squealing frequencies. This is confirmed by monitoring the check-rail acceleration levels and comparing the squealing frequencies involved during the curve negotiation of two tramcars of the same type. The presence of a flange-back contact condition on the leading inner wheel of the vehicle promotes the instability of the axial and radial wheel modes at 1273 and 1423 Hz (3ND) and 2479 Hz (4ND) and at the same time it suppresses squeal of the 535 Hz wheel axial mode with 2ND. Moreover, the flange-back contact seems to favour mode-coupling mechanisms, which are highlighted by squealing frequencies different from the natural frequencies of the wheel vibration modes involved in the squeal events.

Motivated by these experimental findings, a methodology to predict the curve squeal occurrence in the frequency domain, including single and multiple wheel/rail contact points, is formulated to assess the role of this wheel/rail contact condition. A multibody simulation of the reference vehicle is performed for the calculation of the steady-state curving conditions. The wheel dynamic behaviour is introduced by means of a FE model validated against measurements on a resilient wheel of the reference tramcar. The track mobility is introduced by fitting measured mobilities with a ratio of two polynomials. The approach includes vertical-lateral cross terms at each contact point as well as the transfer contribution between different contact points.

Numerical simulations with single and multiple contact conditions show a good agreement with the corresponding occurrences of squealing frequencies measured experimentally. The role of multiple contact points in promoting mode-coupling effects is assessed through squeal simulations in the absence of falling friction. It is shown how the fidelity of curve squeal predictions is strongly related to the accuracy in the description of the actual wheel/rail contact conditions. The use of statistical approaches or sensitivity analysis on different situations is thus recommended to include in the curve squeal prediction all the possible wheel/rail contact conditions.

CRediT authorship contribution statement

Federico Castellini: Conceptualization, Methodology, Software, Validation, Writing – original draft. **Leonardo Faccini:** Conceptualization, Methodology, Software, Writing – review & editing. **Egidio Di Gialleonardo:** Conceptualization, Methodology, Supervision, Writing – review & editing. **Stefano Alfi:** Conceptualization, Methodology, Supervision, Writing – review & editing. **Roberto Corradi:** Conceptualization, Funding acquisition, Methodology, Project administration, Supervision, Writing – review & editing. **Giacomo Squicciarini:** Conceptualization, Methodology, Supervision, Writing – review & editing. **David Thompson:** Conceptualization, Methodology, Supervision, Writing – review & editing.

Table 4
Summary of simulations excluding one or more wheel vibration modes.

Simulation No.	Vibration Modes Removed	Squealing Frequency Range	
		1400–1600 Hz	2400–2600 Hz
1	–	✓	✓
2	Axial 3ND (1273 Hz)	✓	✓
3	Radial 3ND (1423 Hz)		✓
4	Web Axial – 0ND (1560 Hz)	✓	✓
5	Axial 3ND (1273 Hz) Web Axial – 0ND (1560 Hz)		✓
6	Axial 4ND (2479 Hz)	✓	
7	Tyre Torsion – 1ND (2537 Hz)	✓	✓
8	Tyre Radial (2774 Hz)	✓	✓
9	Tyre Torsion – 1ND (2537 Hz) Tyre Radial (2774 Hz)	✓	

Declaration of competing interest

The authors declare that they have no known competing financial interests or personal relationships that could have appeared to influence the work reported in this paper.

Data availability

The data that has been used is confidential.

References

[1] Rudd MJ. Wheel/rail noise-Part II: Wheel squeal. J Sound Vib 1976;46(3):381–94. https://doi.org/10.1016/0022-460X(76)90862-2.

[2] Thompson D. Railway noise and vibration: mechanisms, modelling and means of control. Elsevier 2009. https://doi.org/10.1016/B978-0-08-045147-3.X0023-0.

[3] Hoffmann N, Fischer M, Allgaier R, Gaul L. A minimal model for studying properties of the mode-coupling type instability in friction induced oscillations. Mech Res Commun 2002;29(4):197–205. https://doi.org/10.1016/S0093-6413(02)00254-9.

[4] Meehan PA. Prediction of wheel squeal noise under mode coupling. J Sound Vib 2020;465. https://doi.org/10.1016/J.JSV.2019.115025.

[5] Ding B, Squicciarini G, Thompson D, Corradi R. An assessment of mode-coupling and falling-friction mechanisms in railway curve squeal through a simplified approach. J Sound Vib 2018;423:126–40. https://doi.org/10.1016/J.JSV.2018.02.048.

[6] Lazzari A, Tonazzi D, Brunetti J, Saulot A, Massi F. Contact instability identification by phase shift on C/C friction materials. Mech Syst Signal Process 2022;171. https://doi.org/10.1016/J.YMSSP.2022.108902.

[7] Thompson DJ, Squicciarini G, Ding B, Baeza L. A state-of-the-art review of curve squeal noise: Phenomena, mechanisms, modelling and mitigation. Notes on Numerical Fluid Mechanics and Multidisciplinary Design 2018;139:3–41. https://doi.org/10.1007/978-3-319-73411-8_1.

[8] De Beer FG, Janssens MHA, Kooijman PP. Squeal noise of rail-bound vehicles influenced by lateral contact position. J Sound Vib 2003;267(3):497–507. https://doi.org/10.1016/S0022-460X(03)00710-7.

[9] Huang Z. Theoretical modelling of railway curve squeal. PhD thesis. University of Southampton; 2007. https://scholar.google.com/scholar_lookup?title=Theoretical%20Modelling%20of%20Railway%20Curve%20Squeal&author=Z.%20Huang&publication_year=2007.

[10] Squicciarini G, Usberti S, Thompson DJ, Corradi R, Barbera A. Curve squeal in the presence of two wheel/rail contact points. Notes on Numerical Fluid Mechanics and Multidisciplinary Design 2015;126:603–10. https://doi.org/10.1007/978-3-662-44832-8_71/COVER.

[11] Ding B, Squicciarini G, Thompson D. Effect of rail dynamics on curve squeal under constant friction conditions. J Sound Vib 2019;442:183–99. https://doi.org/10.1016/J.JSV.2018.10.027.

[12] Lai VV, Chiello O, Brunel JF, Dufrénoy P. The critical effect of rail vertical phase response in railway curve squeal generation. Int J Mech Sci 2020;167. https://doi.org/10.1016/J.IJMECSCI.2019.105281.

[13] R. Corradi, A. Facchinetti, S. Manzoni, and M. Vanali, "Effects of track parameters and environmental conditions on tramcar induced squeal noise," in *ISMA2006: International Conference on Noise and Vibration Engineer-ing*, 2006, pp. 3745–3759.

[14] R. Corradi, P. Crosio, S. Manzoni, and G. Squicciarini, "Experimental investigation on squeal noise in tramway sharp curves," *Proceedings of the 8th International Conference on Structural Dynamics, EURODYN 2011*, pp. 3214–3221, 2011.

[15] Meehan PA, Liu X. Modelling and mitigation of wheel squeal noise under friction modifiers. J Sound Vib 2019;440:147–60. https://doi.org/10.1016/J.JSV.2018.10.025.

[16] Ding B. The mechanism of railway curve squeal. University of Southampton; 2018.

[17] Chiello O, Ayasse JB, Vincent N, Koch JR. Curve squeal of urban rolling stock-Part 3: Theoretical model. J Sound Vib 2006;293(3–5):710–27. https://doi.org/10.1016/J.JSV.2005.12.010.

[18] Pieringer A. Time-domain modelling of high-frequency wheel/rail interaction. PhD thesis. Chalmers University of Technology; 2011. https://research.chalmers.se/publication/138969.

[19] Zenzerović I. Time-domain modelling of curve squeal: a fast model for one- and two-point wheel/rail contact. PhD thesis. Chalmers University of Technology; 2017. https://research.chalmers.se/publication/500019.

[20] Martínez-Casas J, Di Gialleonardo E, Bruni S, Baeza L. A comprehensive model of the railway wheelset-track interaction in curves. J Sound Vib 2014;333(18):4152–69. https://doi.org/10.1016/J.JSV.2014.03.032.

[21] Giner-Navarro J, Martínez-Casas J, Denia FD, Baeza L. Study of railway curve squeal in the time domain using a high-frequency vehicle/track interaction model. J Sound Vib 2018;431:177–91. https://doi.org/10.1016/J.JSV.2018.06.004.

[22] Pieringer A. A numerical investigation of curve squeal in the case of constant wheel/rail friction. J Sound Vib 2014;333(18):4295–313. https://doi.org/10.1016/J.JSV.2014.04.024.

[23] Lai VV, Anciant M, Chiello O, Brunel JF, Dufrénoy P. A nonlinear FE model for wheel/rail curve squeal in the time-domain including acoustic predictions. Appl Acoust 2021;179. https://doi.org/10.1016/J.APACOUST.2021.108031.

[24] "BS EN 61672-1:Electroacoustics. Sound level meters - Specifications." 2013.

[25] Belforte P, Cheli F, Corradi R, Facchinetti A. Software for the numerical simulation of tramcar vehicle dynamics. Heavy Vehicle Systems 2003;10(1–2):48–69. https://doi.org/10.1504/ijhvs.2003.002434.

[26] F. Cheli, R. Corradi, and A. Facchinetti, "A numerical model to analyse the dynamic behaviour of modern tramcars," *Proceedings of the Mini Conference on Vehicle System Dynamics, Identification and Anomalies*, pp. 183–190, 2002.

[27] Corradi R, Diana G, Facchinetti A. Sharp curve negotiation analysis of tramcar vehicles with different bogie architectures. Civil-Comp Proceedings 2012;98. https://doi.org/10.4203/CCP.98.129.

[28] Cheli F, Corradi R, Diana G, Facchinetti A. Validation of a numerical model for the simulation of tramcar vehicle dynamics by means of comparison with experimental data. J Comput Nonlinear Dyn 2007;2(4):299–307. https://doi.org/10.1115/1.2754306.

[29] Pascal JP, Sauvage G. The available methods to calculate the wheel/rail forces in non Hertzian contact patches and rail damaging. Veh Syst Dyn 1993;22(3–4):263–75. https://doi.org/10.1080/00423119308969028.

[30] Bruni S, Collina A, Diana G, Vanolo P. Lateral dynamics of a railway vehicle in tangent track and curve: Tests and simulation. Veh Syst Dyn 2000;33:464–77. https://doi.org/10.1080/00423114.1999.12063104.

[31] Knothe K, Stichel S. Rail vehicle dynamics. Rail Vehicle Dynamics 2016:1–321. https://doi.org/10.1007/978-3-319-45376-7.

[32] Mindlin RD. Compliance of elastic bodies in contact. J Appl Mech, Trans ASME 1949;16(3):259–68. https://doi.org/10.1115/1.4009973.

[33] Kraft K. Der einfluß der fahrgeschwindigkeit auf den haftwert zwischen rad und schiene. Arch für Eisenbahntechnik 1967;22:58–78.

[34] Shen ZY, Hedrick JK, Elkins JA. A comparison of alternative creep force models for rail vehicle dynamic analysis. Veh Syst Dyn 1983;12(1–3):79–83. https://doi.org/10.1080/00423118308968725.

[35] Macfarlane AGJ, Postlethwaite I. The generalized nyquist stability criterion and multivariable root loci. Int J Control 1977;25(1):81–127. https://doi.org/10.1080/00207177708922217.

[36] Caverly RJ, Pates R, Bridgeman LJ, Forbes JR. MIMO Nyquist interpretation of the large gain theorem. Int J Control 2020;93(10):2326–35. https://doi.org/10.1080/00207179.2018.1554911.

[37] Wu TX, Thompson DJ. A hybrid model for the noise generation due to railway wheel flats. J Sound Vib 2002;251(1):115–39. https://doi.org/10.1006/JSVI.2001.3980.

[38] Wu TX, Thompson DJ. On the impact noise generation due to a wheel passing over rail joints. J Sound Vib 2003;267(3):485–96. https://doi.org/10.1016/S0022-460X(03)00709-0.

[39] Lewis R, Olofsson U. Wheel-rail interface handbook. Elsevier Ltd 2009. https://doi.org/10.1533/9781845696788.